Dalton Transactions

Accepted Manuscript

ROYAL SOCIETY OF CHEMISTRY

www.rsc.org/dalton

Hybrid photocatalysts using graphitic carbon nitride/cadmium sulfide/reduced graphene oxide (g-C_3N_4/CdS/RGO) for superior photodegradation of organic pollutants under UV and visible-light

Rajendra C. Pawar[1], Varsha Khare[2] and Caroline Sunyong Lee[1]*

[1]Department of Materials Engineering, Hanyang University,

Ansan 426-791, Gyeonggi-do, South Korea

[2]School of Mechanical & Aerospace Engineering, Seoul National University,
Seoul, 151-742, Korea

ABSTRACT

Graphitic carbon nitride (g-C_3N_4) was hybridized with CdS nanoparticles and reduced graphene oxide (RGO) sheets using a facile chemical method, for the application of catalytic photodegradation of Rhodamine B and Congo red dyes under irradiation with UV and visible light. Fourier-transform infrared (FTIR) spectroscopy and X-ray photoemission spectroscopy (XPS) analyses confirmed the formation of pure g-C_3N_4, as well as g-C_3N_4/CdS, g-C_3N_4/RGO, and g-C_3N_4/CdS/RGO composites. The large surface area of the g-C_3N_4/CdS/RGO composite (70.42 m^2g^{-1}) resulted in rapid dye adsorption onto surface of the photocatalyst, leading to effective photodegradation of organic pollutants. The addition of CdS and RGO increased the photocatalytic activity of g-C_3N_4 by a factor of approximately twenty compared with that of commercially available TiO_2 catalyst under visible light, and the g-C_3N_4/CdS/RGO composite was found to significantly enhance the catalytic effect compared with pure g-C_3N_4 and with the g-C_3N_4/CdS and g-C_3N_4/RGO composites. The superior photocatalytic activity of the g-C_3N_4/CdS/RGO composite is attributed to enhanced separation of the photogenerated electron–

hole pairs, as well as increased visible-light absorption. The improved transport of photoelectrons was consistent with the results of transient photocurrent measurements. Therefore, g-C_3N_4/CdS/RGO composites using a facile method, is applicable to the development of high-efficiency photocatalytic devices for industrial applications.

Keywords: Graphitic carbon nitride, Reduced Graphene Oxide, CdS, Photocatalysis

Corresponding Author: Caroline Sunyong Lee (sunyonglee@hanyang.ac.kr)

Introduction

Since the discovery of water splitting by Fujishima and Honda, semiconductor photocatalysis technology has attracted considerable attention because of the potential applications in photodegradation of organic pollutants, self-cleaning, and bacterial elimination using non-toxic, low cost methods [1–5]. This represents one of the most promising technologies to overcome the present energy and water pollution problems. Over the past four decades, various semiconductor photocatalysts, including TiO_2, SnO_2, ZnO, WO_3, Fe_2O_3, Bi_2WO_6, In_2S_3, and BiOBr, have been studied and employed in environmental remediation [5–11]. Despite the high photocatalytic activity and good chemical stability, the application of semiconductor catalysts is limited because of the high rate of recombination of electron–hole pairs, low absorption coefficient, and mismatch with the solar spectrum. Therefore, various approaches, including semiconductor–semiconductor, elemental doping in semiconductor, semiconductor–metal, semiconductor–graphene, and sensitization with visible band-gap semiconductors, have been developed [12–14]. The development of semiconductors that absorb in the visible part of the electromagnetic spectrum and the use of graphene are among the most promising strategies due to the large coverage of the visible region of solar spectrum (40%) and reduced recombination of photogenerated charge carriers. Recently, a polymeric semiconductor, known as graphitic carbon nitride (g-C_3N_4), has been reported with remarkable potential applications in photocatalysis and hydrogen gas production [15]. It exhibits various interesting properties, including visible-light absorption (with a band gap of 2.7 eV), thermal, chemical (acidic and basic solutions), and photochemical stability due to its s-triazine structure, and a high degree of condensation. Moreover, the method of fabrication is simple and low cost (i.e., sintering of nitrogen-rich

compounds such as urea, thiourea, and melamine) [16–19]. Additionally, the band structure may be tailored by modification in the nanostructure and by chemical doping [20].

Nevertheless, bare g-C_3N_4 suffers from an insufficient visible light absorption (can absorb wavelengths < 460 nm), grain boundary effects, and weak van der Waals interaction between two neighboring planes slowing down photoelectron transfer process which leads to high recombination rate, and hence these drawbacks limit its photocatalytic performance [21–23]. Various strategies such as chemical doping and composite with ZnO, WO_3, NiOH, BiOCl, ZnS, Fe_3O_4, $BiVO_4$ and TiO_2 nanostructures, have been reported to overcome these problems [24–31]. These attempts have reduced recombination losses and shown good photocatalytic performance to some extent. Hence, in order to achieve further improvement in g-C_3N_4, there are few attempts made by combining the conducting materials, including reduced graphene oxide (RGO), carbon nanotubes (CNTs), and gold (Au) nanoparticles [32–34]. Among these, RGO appears to be the most promising material for effective transfer of photoelectrons due to its high electron mobility at room temperature, large specific surface area, excellent thermal conductivity, and high Young's modulus [35,36]. RGO has been explored by combining with various semiconductors to develop efficient photocatalysts [37,38]. It was observed that RGO played a crucial role in the effective separation of photogenerated electron–hole pairs. Despite of RGO incorporation, the photocatalytic performance of g-C_3N_4 has not been improved to an extent that it is suitable for industrial or commercial use. Recently, sensitization with visible-band-gap semiconductors, including CdS, CdSe, and PbS, has been shown to be a promising route to enhance photodegradation due to efficient separation of the photogenerated charge carriers [39–42]. Hence, it is expected that CdS could increase the visible absorption due to its direct band gap of 2.4 eV and exhibits Bohr's radius of 2.4 nm. It has been used in various fields including

photocatalysis, quantum dot solar cells, light emitting diodes and optical devices [43,44]. Moreover, its morphology can be controlled easily using chemical methods at low cost, reducing device fabrication cost. From the above discussion of composites, it appears that combining multiple materials allows us to exploit the various material properties, and composite materials may be expected to be particularly suitable for the development of efficient photocatalysts. Thus, a combination of CdS and RGO together with g-C_3N_4 photocatalyst may show superior photocatalytic activity. In a preliminary study, we found that CdS and RGO improved the photodegradation performance of ZnO nanorods due to increased visible absorption and separation of the electron–hole pairs [45,46].

Here, we report g-C_3N_4/CdS/RGO composites fabricated using a facile aqueous chemical method for the photodegradation of Rhodamine B (RhB) and Congo red (CR) dyes under visible irradiation. We measured the photocatalytic activity of pure g-C_3N_4, g-C_3N_4/CdS, g-C_3N_4/RGO, and g-C_3N_4/CdS/RGO composites. The results show that CdS and RGO incorporated with g-C_3N_4 exhibited significantly more rapid photodegradation compared with pure g-C_3N_4 toward RhB and CR under visible light. We discuss possible photocatalysis mechanisms of the composites in detail. The photocatalytic performance and optical properties of the composites were correlated with photocatalysis.

Fabrication and characterization

Materials

Graphite flakes, hydrogen peroxide, hydrazine hydrate (Alfa-Aesar), urea, cadmium sulfate, sulfuric acid, absolute ethanol, and thiourea (Junsei chemicals) were used as received without further purification.

Preparation of g-C_3N_4 powder

To collect g-C_3N_4 powders, the authors followed the method reported in Ref. [47]. In brief, 20 g of urea was place in a ceramic crucible and placed in an oven at 70 ºC for 2 hours. The crucible was then placed in a box furnace and annealed at 580 ºC under air atmosphere for a further 2 hours with the furnace rate set at 5 ºC per minute. After the furnace was allowed to cool to room temperature, the yellow g-C_3N_4 powder was collected in glass vials.

Preparation of RGO sheets

Reduced graphene oxide sheets were synthesized in two steps. First, graphene oxide (GO) sheets were collected using the modified Hummers method [48]. First, 2 g of natural graphite flakes was mixed with 100 ml of sulfuric acid (H_2SO_4) at room temperature and stirred for 2 hours with the temperature maintained below 10 ºC. Then, 8 g of potassium permanganate ($KMnO_4$) was added to this solution and stirred constantly for 2 hours and then diluted with 300 ml of distilled water. Next, 20 ml of hydrogen peroxide (H_2O_2, 30%) was added to the mixture to completely dissolve the $KNMO_4$. This resulted in vigorous bubbling of the solution and a color change to brilliant yellow. Finally, the GO powder was collected using filtration and washing with hydrochloric acid (HCl) and distilled water. In the second step, 100 mg of the GO powder was dispersed in 100 ml of water by sonicating it for 2 hours and then refluxed for 2 hours at 70 ºC with 20 ml of hydrazine hydrate to facilitate the reduction. The solution then changed color to black, indicating the complete reduction of the GO sheets.

Fabrication of g-C_3N_4/CdS, g-C_3N_4/RGO, and g-C_3N_4/CdS/RGO composites

The composites were fabricated using a chemical bath deposition method. Initially, a 100 mg of g-C_3N_4 powder was dispersed in 80 ml of distilled water by ultrasonication for 1 hour. To fabricate the g-C_3N_4/CdS composite, an equimolar quantity of a 0.005 M solution of cadmium sulfate (0.153 g) and thiourea (0.017 g) was added to the g-C_3N_4 dispersion, which was stirred constantly, and the pH of solution was adjusted to 11 by adding ammonia. The solution was heated at 70 ºC for 5 hours while stirring constantly. Powdered g-C_3N_4/CdS was then collected by filtration and washed with distilled water and ethanol. Similar procedure was used to collect RGO/CdS powders. To fabricate the g-C_3N_4/RGO composite, 0.20 wt% RGO (with respect to weight of g-C_3N_4) and 100 mg of g-C_3N_4 were mixed and dispersed in 80 ml distilled water using ultrasonication for 1 hour. The solution was then filtered, and powdered g-C_3N_4/RGO was collected.

To fabricate the g-C_3N_4/CdS/RGO composite, 0.20 wt% RGO and a 100 mg of g-C_3N_4 was dispersed in 80 ml distilled water using ultrasonication, and cadmium sulfate and thiourea were added to the mixture under constant stirring at room temperature. The pH of the mixture was maintained at 11 by adding ammonia, and it was heated at 70 ºC for 5 hours. The powdered g-C_3N_4/CdS/RGO composite was then collected by filtration.

Characterization of Photocatalysts

The phase formation of composite samples was analyzed using X-ray diffraction (XRD) with a Rigaku D/MAX-2500/PC, USA, diffractometer using Cu Kα radiation (λ = 1.5418 Å) at a scan rate (2θ) of 0.04 º s^{-1}. Field emission scanning electron miscopy (FESEM) images were obtained

using a JMIRA3 LM (Tescan, USA) to observe the surface morphology. The detailed microstructure analysis of composite samples was carried out using a high-resolution scanning electron microscope (HRTEM, JEOL, 2100) operated at 200 kV. The formation and purity of the g-C_3N_4 and g-C_3N_4/CdS/RGO composite were confirmed using X-ray photoelectron spectroscopy (XPS) for chemical analysis (ESCA, sigma probe; Thermo-Scientific, UK) at ultrahigh vacuum using a multichannel electron spectrometer with a spherical-sector (180º) electron analyzer with a mean radius of 275 mm. Molecular structural information was inferred from Fourier-transform infrared spectroscopy (FTIR) data (Bruker IFS 66/S) using a standard KBr disk method. The optical absorbance was measured on a UV–VIS spectrophotometer (V-600; Jasco, Japan) with a dry-press disk with $BaSO_4$ used as the reference. Room-temperature photoluminescence (PL) spectra with an excitation wavelength of 325 nm were obtained using a fluorescence spectrophotometer connected with a He–Cd laser (Dong Woo Optron, South Korea). The specific surface area was calculated from N_2 adsorption–desorption isotherms measured using a Quantachrome instrument (AS1, USA) using the Brunauer–Emmett–Teller (BET) equation. The pore-size distributions were obtained from the desorption branches using the Barrett–Joyner–Halenda (BJH) method.

Photocatalytic experiments

A batch-type photoreactor with a 250 mL beaker and a visible-light and UV sources (100 W, Halogen lamp for visible light and 300 W, UV lamp for UV light) was used. The photocatalytic activity toward photodegradation of a 4-mg/L solution of RhB and a 20 mg/L solution of CR was used to characterize the materials. Prior to the measurements, 100 mg of the photocatalyst was dispersed in 250 ml of the dye solution and stirred at room temperature for 1 hour to reach

adsorption–desorption equilibrium. The well-dispersed solutions were maintained under visible irradiation and given time intervals, and 3 ml aliquots were collected and centrifuged to separate the photocatalysts from photodegraded dye solution. Optical absorbance spectra of the samples were measured using a UV–VIS spectrophotometer. Changes in the concentration of RhB and CR were determined by examining changes in the absorbance at 554 nm and 500 nm, respectively. After complete photodegradation of dye solution, the total organic carbon was measured using Shimadzu TOC analyzer (TOC-V_{CSH}, Japan).

Photoelectrochemical (PEC) measurement

Transient photocurrent response measurements were performed using a potentiostat (EG and E175) in a standard three-electrode system with a graphite counter electrode and a saturated calomel reference electrode. A 0.5 M aqueous solution of Na_2SO_4 was used as a redox electrolyte. A halogen lamp was used to illuminate the electrode at an intensity of 5 mW cm^{-2}. The working electrodes, with an area of approximately 1 cm^2, were prepared as follows: 10 mg of photocatalyst powder was added to 1 ml of distilled water and 0.5 ml of Liquion solution to make a slurry, and the powders were dispersed using ultrasonication. A small amount of the solution was injected onto a 2 × 6 cm^2 fluorine-doped tin-oxide (FTO) glass substrate and dried at 60ºC.

XRD analyses

The crystal structure and orientation of composite samples was studied using XRD. Fig. S1 shows a comparison of the XRD patterns for the g-C_3N_4, g-C_3N_4/CdS, g-C_3N_4/RGO, and g-C_3N_4/CdS/RGO samples recorded at diffraction angles in the range 10–80 º. The two distinct

diffraction peaks at 27.8 º and 12.9 º in the XRD patterns of g-C_3N_4 correspond to interlayer stacking of aromatic species and the in-plane order of tri-s-triazine, respectively. These two diffraction peaks are consistent with g-C_3N_4 [49]. Following incorporation of CdS nanoparticles into the g-C_3N_4 networks, the intensity of these two g-C_3N_4 peaks remained approximately constant, and additional peaks related to CdS appeared at 24.83 º, 36.65 º, and 43.72 º, which are attributable to the (100), (102), and (110) planes of hexagonal CdS. In the g-C_3N_4/RGO composite, the two peaks related to g-C_3N_4 at 27.8 º and 12.9 º were identified; however, peaks for RGO were not clearly visible, which is attributed to the relatively low quantity of RGO, consistent with previous reports of XRD characterization of RGO composites [50,51]. The XRD pattern of the g-C_3N_4/CdS/RGO composite exhibited peaks corresponding to g-C_3N_4 and CdS nanoparticles, indicating the formation of a g-C_3N_4 and CdS composite with RGO.

FESEM and TEM analysis

Formation of porous and sheet-like structure of pure g-C_3N_4 sample was studied using FESEM (see Fig. 1a). It can be seen that the obtained pure g-C_3N_4 structure is made up of few nanometer sized sheets and pores. Further, from the magnified FESEM image, it revealed that the g-C_3N_4 sheets were interconnected and small pores were formed in between two adjacent sheets. In g-C_3N_4/CdS composite, the aggregation of CdS particles with a random shape and size were obtained and these were combined throughout the sample with g-C_3N_4 sheet (see Fig. 1b). Therefore, it was difficult to differentiate between these two materials (see the magnified image of Fig. 1b). For the g-C_3N_4/RGO composite, it can be seen that smaller g-C_3N_4 sheets were formed as these were coated on the top surface of RGO, as shown in Fig. 1c. The magnified image of g-C_3N_4/RGO composite indicates that the RGO sheets mixed well with the g-C_3N_4

sheets, which were several nanometers thick (see the magnified image of Fig. 1c). In case of g-C_3N_4/CdS/RGO composite, it can be seen that g-C_3N_4 sheets were formed right at the surface of the RGO, which was distributed uniformly throughout sample (see Fig. 1d). Following incorporation of the CdS nanoparticles (CNPs), most of the g-C_3N_4 sheets were covered with the particles, which had an average diameter of 40 nm (see the magnified image of Fig. 1d). The density of CNPs was high, as was that of the g-C_3N_4 sheets, and the CNPs were distributed over the entire sample with no evidence of aggregation. This indicates that the presence of the RGO sheets may have hindered the aggregation of the CNPs. We have previously analyzed RGO and confirmed the formation of RGO sheets with an extent of several micrometers [52].

Before TEM analysis of composite sample, pure g-C_3N_4 and CdS nanoparticles were analyzed separately (Fig.S2a–d). After the direct condensation of urea in air atmosphere, the sheet-like structure was formed for pure g-C_3N_4 sample. Its nano-crystalline structure was confirmed by SAED pattern. In case of CdS nanoparticles, the random shaped particles with its average diameter of 40 nm, were grown with a polycrystalline structure. Then, the TEM images of g-C_3N_4 and CdS nanoparticles combined with the RGO sheets to form the g-C_3N_4/CdS/RGO composite, are shown in Fig. 2. It can be seen that the CdS nanoparticles and g-C_3N_4 sheets completely covered the RGO sheets; however, the CdS nanoparticles appeared invisible. The presence of micron-sized RGO sheets also confirms that the RGO sheets were largely intact (Fig. 2a). The magnified TEM image in Fig. 2b shows that the CdS nanoparticles were sporadically coated on the g-C_3N_4 and RGO sheets. To confirm the presence of the CdS nanoparticles, we further analyzed the g-C_3N_4/CdS/RGO composite using HR-TEM. Fig. 2c shows that the HRTEM image of CNPs were distributed over the entire g-C_3N_4 and RGO sheets. The measured lattice spacing for crystalline plane of 0.33nm indicated the CdS particles with a hexagonal

crystal structure oriented along (002) direction (JCPDS#01-070-2553). The nano-crystalline nature of CdS particles was confirmed from selected-area electron diffraction (SAED) pattern as shown in Fig. 2d, and it matches with the pattern for pure CdS nanoparticles. The presence of the CdS nanoparticles, g-C_3N_4, and RGO sheets in TEM images, confirms the formation of the g-C_3N_4/CdS/RGO composite. Moreover, the high density of the g-C_3N_4 sheets and CNPs, is expected to enhance optical absorption because of its band-gap energies in visible wavelength, and RGO is expected to minimize recombination losses by allowing separation of the electron–hole pairs.

FTIR analyses

The formation of g-C_3N_4, g-C_3N_4/CdS, g-C_3N_4/RGO, and g-C_3N_4/CdS/RGO composites was further analyzed using FTIR. For comparison, we have provided FTIR spectra of pure CdS, g-C_3N_4, and RGO, as shown in Fig. S3. The absence of peaks related to oxygen-containing functional groups at 1066 cm^{-1} (the stretching mode of C–O) and 1732 cm^{-1} (the stretching mode of C=O) in the RGO spectra, confirms complete reduction of the graphene oxide [53]. However, there were peaks at 1539 cm^{-1}, 3520 cm^{-1}, 1620 cm^{-1}, and 1187 cm^{-1}, which may be attributed to water molecules adsorbed from the air and remaining un-oxidized graphite domains following the reduction process [54–56]. The FTIR spectra of pure CdS nanoparticles exhibit peaks at 2151 cm^{-1}, 1391 cm^{-1}, 1114 cm^{-1} and 652 cm^{-1}, which correspond to Cd–S bond vibrations [57]. The FTIR spectra of pure g-C_3N_4 shows a principle absorption band in the range of 1200–1650 cm^{-1}, which is attributed to stretching vibrational modes of C–N heterocycles [58]. The band at 810 cm^{-1} is attributed to out-of-plane breathing modes of heterocyclic C–N [59]. The strong bands around 3252 cm^{-1} and 3161 cm^{-1} are assigned to the presence of adsorbed water molecules. After

combination of g-C_3N_4 and CdS, the FTIR spectra showed bands related to the g-C_3N_4 and CdS materials, confirming the successful formation of the composite. The FTIR spectra of the g-C_3N_4/RGO composite exhibited bands corresponding to only g-C_3N_4 because of the small amount of RGO in the material. Similarly, the FTIR spectra of g-C_3N_4/CdS/RGO showed bands related to g-C_3N_4 and CdS, which is consistent with the FTIR spectra of these pure materials. Therefore, the FTIR analysis supports the formation of the g-C_3N_4/CdS/RGO composite.

X-ray photoelectron spectroscopy

Elemental analysis of the samples was performed using XPS to confirm the formation of pure g-C_3N_4 and of the g-C_3N_4/CdS/RGO composite. The data shown in Fig. S4a exhibit peaks corresponding to C, N, Cd, and S, confirming the formation of the g-C_3N_4/CdS/RGO composite. The O 1s peak at 532.5 eV was attributed -OH groups at the surface resulting from surface adsorption of oxygen. The strong C 1s peak centered at 288.01 eV was attributed to carbon bonded with nitrogen forming C–N–C (Fig. S4b) [60]. The two peaks at 286.2 eV and 284.5 eV were assigned to graphitic carbon nitrides and C=C bonds from the RGO [56–63]. This confirms the presence of RGO and g-C_3N_4 in the composite. Additionally, there were two peaks at 282.92 eV and 281.16 eV, which correspond to contamination from carbon. The strong peak at 398.3 eV was assigned to sp^2-hybridized aromatic nitrogen bonded to carbon atoms (C=N–C) [64]. The two weak peaks at 400.0 eV and 402.1 eV were assigned to tertiary nitrogen bonded to carbon $(N–C)_3$) and quaternary nitrogen bonded with carbon atoms in an aromatic cycle (C–N–H), respectively (Fig. S4c) [65]. The double-peaked structures observed in the XPS spectra of Cd indicate that the Cd 3d core levels originate from a spin–orbit interaction with the Cd $3d^3$ peak at 404.9 eV and the Cd $3d^5$ peak at 411.7 eV [66]. This doublet Cd spectrum indicates the presence

of a cadmium sulfide phase (Fig. S4c). The peak at 161.7 eV was assigned to S, which was in the form of sulfide (Fig. S4d). These XPS data support the formation of the g-C_3N_4/CdS/RGO composite.

Optical absorbance

The optical properties of pure g-C_3N_4 and its composite with CdS and RGO were investigated by UV–VIS spectrophotometer, as shown in Fig. 3. The strong absorption edge at 450 nm is the result of the intrinsic band-gap energy of g-C_3N_4 (2.7 eV). Compared with pure g-C_3N_4 sample, the g-C_3N_4/CdS composite showed a red-shifted absorption peak at around 500 nm. This is attributed to absorption in the CdS nanoparticles, which have a band gap of 2.4 eV. For the g-C_3N_4/RGO composite, the absorption in the visible region increased substantially, and the absorption edge remained at the original band gap energy of g-C_3N_4. Hence, RGO has improved absorption in the visible spectrum. The absorption of the g-C_3N_4/CdS/RGO composite in visible region was almost the same as that of g-C_3N_4/CdS, but with an additional edge at around 500 nm, which is related to the CdS nanoparticles. Hence, incorporation of CdS nanoparticles as well as RGO sheets increased absorption in the visible region of the electromagnetic spectrum.

Photoluminescence measurements

Effective charge separation and transport can be determined from room temperature photoluminescence (PL) spectra. Figure 4 shows PL spectra of pure g-C_3N_4, g-C_3N_4/CdS, g-C_3N_4/RGO, and g-C_3N_4/CdS/RGO samples measured at an excitation wavelength of 325 nm. It can be seen that the pure g-C_3N_4 and its composites exhibit similar emission trends, with the principle peak around 450 nm, which is attributed to n-π^* electronic transitions [67,68]. The energy of this peak was approximately equal to the band-gap energy of g-C_3N_4 (i.e., 2.7 eV). The

pure g-C_3N_4 sample was found to have a higher PL intensity than the composites. This indicates that g-C_3N_4 had the highest optical recombination rate, which may deteriorate the photodegradation efficiency. However, PL quenching was observed in the composites, and it was most significant in g-C_3N_4/CdS/RGO, which indicates that this composite had a lower rate of recombination of photoelectrons compared with pure g-C_3N_4 and the other composites. The low emission of g-C_3N_4/CdS/RGO composite is attributed to the electron transfer capability of the RGO sheets because of high charge-carrier mobility. Xiang *et al*. showed that graphene sheets can effectively separate photoelectrons from the g-C_3N_4 sheets [32]. In our earlier report, we found that RGO reduced the recombination losses by capturing photoelectrons from a semiconductor [43]. Hence, we believe that the g-C_3N_4/CdS/RGO composite will degrade organic pollutants more rapidly than will either the pure g-C_3N_4 or the other composites.

Surface area and pore-size distribution

To determine the adsorption capacity toward organic pollutants, we measured the Brunauer–Emmett–Teller (BET) surface area of pure g-C_3N_4, as well as the composites, using liquid nitrogen adsorption–desorption isotherms. Figures 5a–d show the isotherm curves of pure g-C_3N_4 and of the g-C_3N_4/CdS, g-C_3N_4/RGO, and g-C_3N_4/CdS/RGO composites, together with the corresponding pore-size distribution calculated using the BJH method (see the inset of Figs. 7a–d). The specific surface area of all the samples is shown in the figures. The g-C_3N_4/CdS/RGO composite was found to exhibit the largest surface area, 70.42 m^2g^{-1}; the surface area of the pure g-C_3N_4 was 47.80 m^2g^{-1}, that of g-C_3N_4/CdS was 51.56 m^2g^{-1}, and that of g-C_3N_4/RGO was 55.62 m^2g^{-1} (see Table 1). The increase in the surface is related to the combination of RGO and CdS nanoparticles with the g-C_3N_4 sheet. Xu *et al*. synthesized nanoporous g-C_3N_4 using a

bubble template method; they obtained a surface area of 29.5 m^2g^{-1} and showed improved photocatalytic activity [69]. In the present work, we obtained composites with specific surface areas higher than those reported previously [70]. We therefore believe that g-C_3N_4 and its composites will degrade organic pollutants in visible light more effectively than has been reported previously. Furthermore, the pore-size distributions of the samples reveal that the pure g-C_3N_4 was macroporous, and it became mesoporous following RGO and CdS sensitization. This is consistent with a uniform distribution of CdS nanoparticles on the RGO and the g-C_3N_4 sheet.

Results and discussion

Photocatalytic degradation of Rhodamine B under visible irradiation

The photocatalytic activity of pure g-C_3N_4, as well as the composites with CdS and RGO, was assessed by degrading Rhodamine B (RhB) and Congo red (CR) solutions under irradiation with visible light. Moreover, dark adsorption was measured for 30 minutes of dye molecules to check self degradation. As a result, the optical absorbance remained almost the same for pure and composite samples indicating that there is no adsorption in the dark. Figure S5a–e shows the optical absorbance of the RhB solution degraded using different photocatalysts. It can be observed that g-C_3N_4/CdS/RGO degraded the dye almost completely within 60 minutes, which is three to four times faster than that of pure g-C_3N_4 (>170 minutes) or the g-C_3N_4/CdS (170 minutes) or RGO/CdS (150 minutes) and g-C_3N_4/RGO (120 minutes) composites. However, pure g-C_3N_4 was found to degrade only half of the initial quantity of RhB. From optical the absorbance curves, we observed two mechanisms of photodegradation. The first was the decrease in the optical absorbance due to photodegradation of the RhB molecule; the second was a hypsochromic shift of the absorption peak over time as the sample was exposed to visible light,

which is attributed to an N-deethylation process [71]. This phenomenon occurred because of self-photodegradation of RhB on the surface of the photocatalyst [72]. The photocatalytic activities of the pure and composite samples were analyzed by plotting the relative absorbance 100 $A_0/A(t)$, where A_0 is the absorbance before irradiation, and $A(t)$ is the absorbance of the dye solution as a function of the irradiation time (Fig. 6a). Photodegradation of RhB without any catalyst and with Degussa P25 powder (TiO_2) were used as a control. With no catalyst, a slight decrease in the RhB concentration was observed after the visible-light irradiation. However, the RhB concentration decreased considerably in the presence of the catalysts. The g-C_3N_4/CdS/RGO composite exhibited superior photocatalytic activity to the other composites, as well as to pure g-C_3N_4. The improved photocatalytic activity of the g-C_3N_4/CdS/RGO composite is attributed to reduced recombination losses compared with pure g-C_3N_4.

We have analyzed the photodegradation properties of the materials by calculating the kinetic rate constant from $\ln(A_0/A(t))$ vs. t, where k is the gradient of this curve, i.e., the apparent kinetic rate constant [73]. The linear curve shown in Fig. 6b illustrates that first order reaction kinetics apply, which follow the Langmuir–Hinshelwood model. The kinetic rate constant for g-C_3N_4/CdS/RGO was found to be k = 21.92 min^{-1}, which is almost twenty times larger than that of P25 (k = 0.96 min^{-1}) and was the highest among all g-C_3N_4-based samples. The rate constants of the pure g-C_3N_4 (k = 1.77 min^{-1}), g-C_3N_4/CdS (k = 6.43 min^{-1}), RGO/CdS (k = 9.31 min^{-1}), and g-C_3N_4/RGO (k = 10.49 min^{-1}) were all larger than that of the P25 powder, but were significantly smaller than that of the g-C_3N_4/CdS/RGO composite (Table 1). Further, TOC concentration after photodegradation of dye was measured to confirm the complete degradation of dye molecules (Table 2). The similar trend in TOC was found as that of optical absorbance.

It is known that photodegradation performance of catalysts largely depends on the recombination and transport of photogenerated charge carriers, the optical absorbance, and the available surface area for dye adsorption on the surface of the catalyst. We found that the g-C_3N_4/CdS/RGO composite exhibited the largest optical absorbance and specific surface area of the g-C_3N_4-based materials. Due to large electron mobility of the RGO, captured photoelectrons from the CdS and g-C_3N_4 semiconductors may be effectively transported, resulting in reduced electron–hole recombination, which was consistent with the PL quenching observations.

Photocatalytic degradation of Rhodamine B under UV irradiation

After visible irradiation, UV photocatalytic activity of the prepared composites under same conditions was investigated as that for the visible light. Figure S6a–e shows the optical absorbance of RhB over different time of irradiation in presence of photocatalysts under UV irradiation. It was shown that the peak intensity of RhB decreased quickly and completely diminished within 20 minutes for g-C_3N_4/CdS/RGO composite which is three times shorter than the one for pure g-C_3N_4 (60 minutes), g-C_3N_4/CdS (40 minutes), RGO/CdS (40 minutes) and g-C_3N_4/RGO (30 minutes) composites. The short photodegradation time of RhB might be due to its high energy of UV rather than that of visible light. As shown in Fig. 6c which is an overall comparison of relative absorbance, RhB degradation in the absence of photocatalyst is very slow. The removal efficiency of g-C_3N_4/CdS/RGO composite is higher than those of the other composites and pure g-C_3N_4. Trend of these results is very similar to the cases with visible photocatalytic activity. However, the photocatalytic activity of P25 is high or similar to that of g-C_3N_4/CdS/RGO composite, attributed to its band gap energy (3.2 eV) which absorbs UV light effectively. For the further analysis of these composites under UV light, kinetic rate constant

from logarithmic plots was plotted as shown in Fig. 6d. A summary of the results is provided in Table 2. It was observed that the calculated rate constant of g-C_3N_4/CdS/RGO composite (k = 66.12 min^{-1}) is high, compared to those of the pure g-C_3N_4 (k = 23.85 min^{-1}), g-C_3N_4/CdS (k = 36.09 min^{-1}), RGO/CdS (k = 38.55 min^{-1}), and g-C_3N_4/RGO (k = 46.02 min^{-1}) composites and P25 (k = 48.98 min^{-1}) powders. It clearly demonstrated that RGO and CdS improved the photocatalytic activity of pure g-C_3N_4 due to its high rate of photoelectrons transfer and specific surface area for dye photodegradation. TOC analyses of photodegraded RhB under UV light, are provided in Table 2. It was seen that g-C_3N_4/CdS/RGO composite and P25 powders, have the lowest amount of carbon concentration remaining, compared to those of other composites and pure g-C_3N_4. Therefore, RGO sheet and CdS nanoparticles improved photocatalytic activity of g-C3N4 due to its high absorption and transportation of photogenerated electrons.

Photocatalytic degradation of Congo Red (CR) under visible irradiation

To use g-C_3N_4-based composites in a wide range of photodegradation applications, the photodegradation of CR dye under irradiation with visible light, was explored. All measurements were performed under the same conditions as those for RhB experiment. As shown in Figure S7a–e, it was clear that the g-C_3N_4/CdS/RGO composite required less time (40 minutes) than those for pure g-C_3N_4, g-C_3N_4/CdS, RGO/CdS and g-C_3N_4/RGO composites, to degrade the dye. CR photodegradation was analyzed using the relative absorbance and logarithmic plots as shown in Figures 7a and 7b. The photocatalytic activities with no catalyst and with P25 powders, are shown for comparison. It is clear that no photodegradation occurred in the absence of a catalyst, and where a catalyst was used, complete degradation of the dye was observed. The kinetic rate constant calculated from logarithmic plots was found to be k = 24.37 min^{-1} for g-C_3N_4/CdS/RGO

composite compared to $k = 1.91$ min^{-1} for P25, $k = 3.24$ min^{-1} for pure g-C_3N_4, $k = 4.06$ min^{-1} for the g-C_3N_4/CdS composite, $k = 5.56$ min^{-1} for the RGO/CdS composite, and $k = 14.80$ min^{-1} for the g-C_3N_4/RGO composite. The g-C_3N_4/CdS/RGO composite resulted significantly faster photodegradation of the CR dye compared to the other materials. That is consistent with the photocatalytic degradation results for RhB. After visible photodegradation of CR, we have analyzed remaining solution using TOC analyzer as shown in Table 2. It revealed that the CR solution degraded with g-C_3N_4/CdS/RGO composite, resulting the lowest amount of carbon concentration among all the samples. The trend of these results matches with that for RhB photocatalytic activity under UV and visible light.

Photocatalytic degradation of Congo Red under UV irradiation

Finally, we have studied the photocatalytic activity of prepared composites under UV irradiation towards CR degradation, and its corresponding UV-VIS optical absorbance plots are depicted in Figure S8a–e. As seen from the optical absorbance results, the CR solution irradiated with UV light, degraded within 15 minutes for g-C_3N_4/CdS/RGO composite, and that is shorter time compared to those of the other composites. These results were further analyzed by plotting relative absorbance graphs (Fig. 7c) and calculating kinetic rate constants from logarithmic plots (Fig. 7d). The photodegradation of CR with P25 and activity without any catalysts, are given for comparison. Apparently, the calculated kinetic rate constant for g-C_3N_4/CdS/RGO composite showed the highest value i.e. 50.90 min^{-1}, which is almost double than that of pure g-C_3N_4. (Table 1). However, the kinetic rate constant for P25 powder (45.33 min^{-1}) sample was found to be almost similar with that of g-C_3N_4/CdS/RGO composite which was attributed to band gap energy of P25 in UV region. The photodegraded CR solution was further analyzed using TOC

analyzer as its results are summarized in Table 2. As a result, the lowest TOC concentration for g-C_3N_4/CdS/RGO composite revealed that the composition of g-C_3N_4, CdS and RGO, is suitable for superior CR photodegradation, compared to any other combination of composites or pure g-C_3N_4.

Mechanism of enhanced photocatalysis

During photocatalysis process, it is known that under irradiation condition, oxygen species such as superoxide radical ($O_2^{\cdot-}$), hydroxide radical ($OH^{\cdot}$) and hydrogen peroxide (H_2O_2), initiate the photodegradation reactions. These radicals are produced by photocatalytic reduction of oxygen and oxidation of water. The photocatalytic activity of catalyst depends on its ability to reduce and oxidize photoelectrons and holes generated under irradiation. For the present g-C_3N_4/CdS/RGO composite, the photogenerated electrons from g-C_3N_4 (–3.38 eV) can transfer easily through conduction of CdS (–3.98 eV) and then get captured by RGO (–4.4 eV) sheet due to their suitable energy levels [28,49]. The captured electrons were utilized for reduction of oxygen$(O_2/O_2^{\cdot-}) = -0.16$ eV. Therefore, the conduction band level of g-C_3N_4 is suitable for the generation of superoxide radicals and subsequently OH radicals. However, the valence band level of g-C_3N_4 (1.57 eV) is not sufficient for direct oxidation of H_2O (2.7 eV) molecules through oxidation process. Hence, $OH^{\cdot}$ radicals could be generated from superoxide radicals [74–79]. Schematic 1 shows possible routes of photoelectron generation and transport in the g-C_3N_4/CdS/RGO composite.

$$g-C_3N_4 + CdS + graphene \xrightarrow{hv} g-C_3N_4(h^+_{VB}) + CdS(e^-_{CB}) + graphene(e^-) \quad (1)$$

$$graphene(e^-) + O_2 \rightarrow graphene + O_2^- \quad (2)$$

$$.O_2^- + HO_2 + H^+ \rightarrow H_2O_2 + O_2 \qquad (3)$$

$$H_2O_2 + .O_2^- \rightarrow .OH + OH^- + O_2 \qquad (4)$$

$$H_2O_2 + e_{CB}^- \rightarrow .OH + OH^- \ . \qquad (5)$$

Because of the visible-wavelength band-gap energy of g-C_3N_4, it absorbs visible light and generates electron–hole pairs when the photon energy is greater than approximately 2.7 eV (Eq.1). Photogenerated electrons are then transferred toward the conduction band of CdS and to the RGO sheets (Eq. 2). Then these electrons were captured by the RGO sheet react with oxygen to form transient superoxide radicals and superoxide molecules (Eq. 3). Highly reactive -OH radicals form, which mineralize RhB and CR molecules, as shown in Eqs. 4 and 5. Therefore, CdS and RGO play important roles in minimizing the recombination losses and thereby enhancing the photodegradation.

The role of CdS nanoparticles and RGO sheets incorporated with the g-C_3N_4 network was further investigated by measuring the transient photocurrent response of pure g-C_3N_4, g-C_3N_4/CdS, g-C_3N_4/RGO, and g-C_3N_4/CdS/RGO under irradiation with visible light. The results are shown in Fig. 8; the photocurrent rapidly increased following the start of irradiation and returned to zero when the light source was switched off. As shown, the results exhibited repeatability over the five cycles, indicating that both the pure g-C_3N_4 and the composites were photochemically stable. It is interesting to note that current density of the g-C_3N_4/CdS/RGO composite (175 μA/cm^2) was almost twelve times larger than that of pure g-C_3N_4. These results are consistent with the photodegradation data described above.

In order to determine the photo stability of g-C_3N_4/CdS/RGO composite under UV and visible light, the cyclic performance was measured upto three cycles (Fig.9). It is clearly seen that g-C_3N_4/CdS/RGO composite exhibits no noticeable change in photodegradation efficiency, although there is infinitesimal decline in performance as compared with that of first cycle. These results confirmed that g-C_3N_4/CdS/RGO composite has good stability and could be used in a device for water purification application.

Conclusions

We have described enhanced photocatalysis using a g-C_3N_4/CdS/RGO composite. A facile aqueous chemical method was used to fabricate the composite material, which exhibited superior photodegradation of RhB and CR dyes under irradiation with UV and visible light. The improved photocatalytic performance was attributed to a reduction in the recombination rate of the photogenerated electron–hole pairs, as well as increased absorption due to the addition of RGO and CdS addition. Characterization using XRD, FESEM, TEM, PL, XPS, and optical absorbance confirmed the formation of well-ordered g-C_3N_4/CdS/RGO composites. TOC analysis confirms the almost complete photodegradation of RhB and CR dyes under UV and VIS irradiation. Transient photocurrent measurements indicated an increase in the charge-carrier mobility of the material, associated with a reduction in the recombination rate of photogenerated electron–hole pairs. These g-C_3N_4/CdS/RGO composite photocatalysts, which exhibit superior photocatalytic activity compared with existing materials, may have applications in the fabrication of commercial and industrial photocatalytic devices.

Acknowledgments

This research was supported by the Basic Science Research Program of the National Research Foundation of Korea (NRF) funded by the Ministry of Education, Science and Technology (NRF-2012R1A1A3004290), by the NRF grant funded by the Korea government (MEST) (No. 2012R1A2A2A01047189), by the Human Resources Development program (No. 20124030200130) of the Korea Institute of Energy Technology Evaluation and Planning (KETEP) grant funded by the Korea government Ministry of Trade, Industry and Energy. The authors thank Dr. C.H. Ahn and Prof. H.K. Cho from Sungkyunkwan University for their assistance with the room temperature photoluminescence, and Prof. Jai-Sung Lee and Mr. Gilsu Han from Hanyang University for their assistance in optical absorbance measurements.

References

[1] A. Fujishima and K. Honda, Nature, 1972, **238,** 37–38.

[2] A. Fujishima, X. Zhang and D.A. Tryk, Int. J. Hydrogen Energy 2007, **32,** 2664–2672.

[3] M. R. Hoffmann, S.T. Martin, W. Choi and D.W. Bahnemann, Chem. Rev., 1995, **95,** 69–96.

[4] N. Meng, K. H. Leung, Y. C. Leung and K. Sumathy, Renew. Sust. Energy Rev., 2007, **11,** 401–425.

[5] M. Mecklenburg, A. Schuchardt , Y. K. Mishra, S. Kaps, R. Adelung, A. Lotnyk, L. Kienle, and K. Schulte, Adv. Mater., 2012, **24,** 3486–3490.

[6] A. Kubacka, M. F. Garcia and G. Colon, Chem. Rev., 2012, **112,** 1555–1614.

[7] M. Batzill, Energy Environ. Sci., 2011, **4,** 3275–3286.

[8] D. Chen and J. Ye, Adv. Funct. Mater., 2008, **18,** 1922–1928.

[9] K. Sivula, F. L. Formal and M. Gratzel, ChemSusChem, 2012, **4,** 432–449.

[10] T. Reimer, I. Paulowicz, R. Roder, S. Kaps, O. Lupan, S. Chemnitz, W. Benecke, C. Ronning, R. Adelung and Y. K. Mishra, ACS Appl. Mater. Interfaces, 2014, **6,** 7806–7815.

[11] Y. K. Mishra, S. Kaps, A. Schuchardt, I. Paulowicz, X. Jin, D. Gedamu, S. Freitag, M. Claus, S. Wille, A. Kovalev, S. N. Gorb and R. Adelung, Part. Part. Syst. Charact. 2013, **30,** 775–783.

[12] W. Hou and S. B. Cronin, Adv. Funct. Mater., 2012, **23,** 1612–1619.

[13] A. Fujishima and X. Zhang, C. R. Chimie, 2006, **9,** 750–760.

[14] O. M. Alfano, D. Bahneman, A. E. Cassano, R. Dillert and R. Goslich, Catal. Today, 2000, **58,** 199–230.

[15] X. Wang, K. Maeda, A. Thomas, K. Takanabe, G. Xin, J. M. Carlsson, K. Domen and M. A. Antonietti, Nat. Mater., 2009, **8,** 76–80.

[16] X. Li, S. Zhang and Q. Wang, Phys. Chem. Chem. Phys., 2013, **15,** 7142–7146.

[17] X. Wang, S. Blechert and M. Antonietti, ACS Catal., 2012, **2,** 1596–1606.

[18] D. S. Su, J. Zhang, B. Frank, A. Thomas, X. Wang, J. Paraknowitsch and R. Schlogl, ChemSusChem, 2010, **3,** 169–180.

[19] Y. Wang, X. Wang and M. Antonietti, Angew. Chem., Int. Ed., 2012, **51,** 68–89.

[20] S. Chu, Y. Wang, Y. Guo, J. Feng, C. Wang, W. Luo, X. Fan and Z. Zou, ACS Catal., 2013, **3,** 912–919.

[21] Y. Zhang and M. Antonietti, Chem. Asian J., 2010, **5,** 1307–6763.

[22] Y. Zhang, T. Mori, J. Ye and M. Antonietti, J. Am. Chem. Soc., 2010, **132,** 6294–6295.

[23] Y. Li, H. Zhang, P. Liu, D. Wang, Y. Li and H. Zhao, Small, 2013, **9,** 3336 –3344.

[24] J. X. Sun, Y. P. Yuan, L. G. Qiu, X. Jiang, A. J. Xie, Y. H. Shen and J. F. Zhu, Dalton Trans., 2012, **41,** 6756–6763.

[25] L. Huang, H. Xu, Y. Li, H. Li, X. Cheng, J. Xia, Y. Xu and G. Cai, Dalton Trans., 2013, **42,** 8606–8616.

[26] F. Dong, Y. Sun, L. Wu, M. Fu and Z. Wu, Catal. Sci. Technol., 2012, **2,** 1332–1335.

[27] J. Yu, S. Wang, B. Cheng, Z. Lin and F. Huang, Catal. Sci. Technol., 2013, **3,** 1782–1789.

[28] X. Bai, L. Wang, R. Zong and Y. Zhu, J. Phys. Chem., 2013, **117,** 9952–9961.

[29] Y. Tian, B. Chang, J. Lu, J. Fu, F. Xi and X. Dong, ACS Appl. Mater. Inter., 2013, **5,** 7079–7085.

[30] S. Ye, L. G. Qiu, Y. P. Yuan, Y. J. Zhu, J. Xia and J. F. Zhu, J. Mater. Chem., A 2013, **1,** 3008–3015.

[31] J. Zhang, M. Zhang, S. Lin, X. Fu and X. Wang, J. Catal., 2013, **310,** 24–30.

[32] Q. Xiang, J. Yu and M. Jaroniec, J. Phys. Chem. C, 2011, **115,** 7355–7363.

[33] Y. Xu, H. Xu, L. Wang, J. Yan, H. Li, Y. Song, L. Huang and G. Cai, Dalton Trans., 2013, **42,** 7604–7613.

[34] N. Cheng, J. Tian, Q. Liu, C. Ge, A. H. Qusti, A. M. Asiri, A. O. Al-Youbi and X. Sun, ACS Appl. Mater. Inter., 2013, **5,** 6815–6819.

[35] W. Fan, Q. Lai, Z. Zhang and Y. Wang, J. Phys. Chem. C, 2011, **115,** 10694 –10701.

[36] Y. Sun, Q. Wu and G. Shi, Energy Environ. Sci., 2011, **4,** 1113–1132.

[37] Q. Xiang, J. Yu and M. Jaroniec, Chem. Soc. Rev., 2012, **41,** 782–796.

[38] W. Tu, Y. Zhou and Z. Zou, Adv. Funct. Mater., 2013, **23,** 4996–5008.

[39] S. A. Vanalakar, R. C. Pawar, M. P. Suryawanshi, S. S. Mali, D. S. Dalavi, A. V. Moholkar, K. U. Sim, Y. B. Kown, J. H. Kim and P. S. Patil, Mater. Lett., 2011, **65,** 548–551.

[40] P. V. Kamat, J. Phys. Chem. C, 2008, **112,** 18737–18753.

[41] J. Fu, B. Chang, Y. Tian, F. Xi and X. Dong, J. Mater. Chem. A, 2013, **1,** 3083–3090.

[42] L. Ge, F. Zuo, J. Liu, Q. Ma, C. Wang, D. Sun, L. Bartels and P. Feng, J. Phys. Chem. C, 2012, **116,** 13708−13714.

[43] S. Xiong, B. Xi and Y. Qian, J. Phys. Chem. C, 2010, **114,** 14029–14035.

[44] D. Lang, Q. Xiang, G. Qiu, X. Feng and F. Liu, Dalton Trans., 2014, **43,** 7245−7253.

[45] R. C. Pawar and C. S. Lee, Appl. Catal. B Environ., 2014, **144,** 57–65.

[46] R. C. Pawar, J. Y. Lee, E. J. Kim, H. S. Kim and C. S. Lee, Kor. J. Mater. Res., 2012, **22,** 504–507.

[47] J. Liu, T. Zhang, Z. Wang, G. Dawson and W. Chen, J. Mater. Chem., 2011, **21,** 14398–14401.

[48] S. Stankovich, D. A. Dikin, R. D. Piner, K. A. Kohlhaas, A. Kleinhammes, Y. Jia, Y. Wu, S. T. Nguyen and R. S. Ruoff, Carbon, 2007, **45,** 1558–1565.

[49] S. C. Yan, Z. S. Li and Z. G. Zou, Langmuir, 2009, **25,** 10397–10401.

[50] R. C. Pawar, D. Cho and C. S. Lee, Curr. Appl. Phys., 2013, **13,** S50–S57.

[51] Y. L. Chen, Z. A. Hu, Y. Q. Chang, H. Q. Wang, Z. Y. Zhang, Y. Y. Yang, H. Y. Wu, J. Phys. Chem. C, 2011, **115,** 2563–2571.

[52] R. C. Pawar and C. S. Lee, Mater. Chem. Phys., 2013, **141,** 686–693.

[53] Y. Guo, X. Sun, Y. Liu, W. Wang, H. Qiu and J. Gao, Carbon, 2012, **50,** 2513–2523.

[54] A. Prakash, S. Chandra and D. Bahadur, Carbon, 2012, **50,** 4209–4219.

[55] J. Li, H. Lin, Z. Yang and J. Li, Carbon, 2011, **49,** 3024–3030.

[56] C. Nethravathi and M. Rajamathi, Carbon, 2008, **46,** 1994–1998.

[57] S. S. Liji, M. V. Devi, T. P. Sastry and A. B. Mandal, J. Nanopart. Res., 2011, **13,** 1747–1757.

[58] G. Liao, S. Chen, X. Quan, H. Yu and H. Zhao, J. Mater. Chem., 2012, **22,** 2721–2726.

[59] S. Yang, Y. Gong, J. Zhang, L. Zhan, L. Ma, Z. Fang, R. Vajtai, X. Wang and P. M. Ajayan, Adv. Mater., 2013, **25,** 2452–2456.

[60] A. Thomas, A. Fischer, F. Goettmann, M. Antonietti, J. O. Muller, R. Schlogl, J. M. Carlsson, J. Mater. Chem., 2008, **18,** 4893–4908.

[61] Q. Liu and J. Zhang, Langmuir, 2013, **29,** 3821–3828.

[62] W. Wang, J. C. Yu, D. Xia, P. K. Wong and Y. Li, Environ. Sci. Technol., 2013, **47,** 8724–8732.

[63] Y. Sun, C. Li, Y. Xu, H. Bai, Z. Yao and G. Shi, Chem. Comm., 2010, **46,** 4740–4742.

[64] S. Yang, X. Feng, X. Wang and K. Mullen, Angew. Chem., 2011, **123,** 5451–5455.

[65] G. Dong and L. Zhang, J. Mater. Chem., 2012, **22,** 1160–1166.

[66] S. A. Vanalakar, S. S. Mali, R. C. Pawar, N. L. Tarwal, A. V. Moholkar, J. A. Kim, Y. B. Kwon, J. H. Kim and P. S. Patil, Electrochim. Acta, 2011, **56,** 2762–2768.

[67] A. B. Jorge, D. J. Martin, M. T. Dhanoa, A. S. Rahman, N. Makwana, J. Tang, A. Sella, F. Cora, S. Firth, J. A. Darr and P. F. McMillan, J. Phys. Chem. C, 2013, **117,** 7178–7185.

[68] Y. Zhang, J. Liu, G. Wu and W. Chen, Nanoscale, 2012, **4,** 5300–5303.

[69] J. Xu, Y. Wang and Y. Zhu, Langmuir, 2013, **29,** 10566–10572.

[70] J. Mao, T. Peng, X. Zhang, K. Li, L. Ye and L. Zan, Catal. Sci. Technol., 2013, **3,** 1253–1260.

[71] M. A. Behnajady, N. Modirshahla, S. B. Tabrizi and S. Molanee, J. Hazard. Mater., 2008, **152,** 381–386.

[72] J. Hou, C. Y. Yang, Z. Wang, S. Jiao and H. Zhu, Appl. Catal. B Environ., 2013, **129,** 333–341.

[73] R. C. Pawar, H. S. Kim and C. S. Lee, Scripta Mater., 2013, **68,** 142–145.

[74] S. Yang, W. Zhou, C. Ge, Z. Liu, Y. Feng and Z. Li, RSC Adv., 2013, **3,** 5631–5638.

[75] Y. Zhang, Z. R. Tang, X. Fu and Y. J. Xu, ACS Nano, 2011, **5,** 7426–7435.

[76] N. Zhang, Y. Zhang, X. Pan, M. Q. Yang and Y. J. Xu, J. Phys. Chem. C, 2012, **116,** 18023–18031.

[77] T. F. Yeh, J. Cihlar, C. Y. Chang, C. Cheng and H. Teng, Mater. Today, 2013, **16,** 78–84.

[78] M. Q. Yang, N. Zhang and Y. J. Xu, ACS Appl. Mater. Inter., 2013, **5,** 1156–1164.

[79] F. Su, S. C. Mathew, G. Lipner, X. Fu, M. Antonietti, S. Blechert and X. Wang, J. Am. Chem. Soc., 2010, **132,** 16299–16301.

The English in this document has been checked by at least two professional editors, both native speakers of English. For a certificate, please see:

http://www.textcheck.com/certificate/BDUzzJ

Figure Captions

Fig. 1. FE-SEM images. (a) g-C_3N_4 sheets distributed over the surface of the RGO sample at magnifications of 25,000x and 100,000x. (b) The g-C_3N_4 and CdS (0.005 M) combined using a chemical route at magnifications of 25,000x and 100,000x. (c) The g-C3N4/RGO composite (0.20 wt%) combined using ultrasonication for 1 hour at magnifications of 25,000x and 100,000x. (d) The g-C_3N_4/CdS/RGO composite at magnifications of 25,000x and 100,000x.

Fig. 2. (a) TEM image of the g-C_3N_4/CdS/RGO composite with 0.005 M CdS and 0.20 wt% RGO sheets. (b) A magnified TEM image showing the CdS nanoparticles on the g-C_3N_4 sheets, (c) HR-TEM image of CdS particles showing interplanar spacing of 0.33 nm oriented along (002) direction and (d) SAED pattern of corresponding area revealed crystalline structure of CdS.

Fig. 3. Optical absorbance spectra of pure g-C_3N_4, and the g-C_3N_4/CdS, g-C_3N_4/RGO and g-C_3N_4/CdS/RGO composites.

Fig. 4. Room temperature photoluminescence spectra recorded in the range 350–750 nm with an excitation wavelength of 325 nm for pure g-C_3N_4 and the g-C_3N_4/CdS, g-C_3N_4/RGO, and g-C_3N_4/CdS/RGO composites.

Fig. 5. The BET surface area calculated from nitrogen adsorption–desorption isotherms. The insets show the corresponding pore-size distribution. (a) Pure g-C_3N_4, (b) g-C_3N_4/CdS, (c) g-C_3N_4/RGO, and (d) g-C_3N_4/CdS/RGO.

Fig. 6. (A) Relative optical absorbance and (B) $\ln(A_0/A(t))$ for P25, pure g-C_3N_4, and the g-C_3N_4/CdS, RGO/CdS, g-C_3N_4/RGO, and g-C_3N_4/CdS/RGO composites as a function of visible irradiation time. The absorbance of the RhB solution under visible-light irradiation without a

catalyst is shown for comparison, (C) Relative optical absorbance and (D) $\ln(A_0/A(t))$ for RhB photodegradation without catalyst and with P25, pure g-C_3N_4, g-C_3N_4/CdS, RGO/CdS, g-C_3N_4/RGO, and g-C_3N_4/CdS/RGO as a function of UV irradiation time respectively.

Fig. 7. (A) Relative optical absorbance and (B) $\ln(A_0/A(t))$ for Congo red photodegradation without catalyst and with P25, pure g-C_3N_4, g-C_3N_4/CdS, RGO/CdS, g-C_3N_4/RGO, and g-C_3N_4/CdS/RGO as a function of visible irradiation time, (C) Relative optical absorbance and (D) $\ln(A_0/A(t))$ for Congo Red photodegradation without catalyst and with P25, pure g-C_3N_4, g-C_3N_4/CdS, RGO/CdS, g-C_3N_4/RGO, and g-C_3N_4/CdS/RGO as a function of UV irradiation time respectively.

Fig. 8. Transient photocurrent responses of pure g-C_3N_4, g-C_3N_4/CdS, g-C_3N_4/RGO and g-C_3N_4/CdS/RGO recorded under excitation with visible light in an 0.5M Na_2SO_4 electrolyte.

Fig. 9. Cycling test of g-C_3N_4/CdS/RGO composite up to 3 times under VIS (bars with vertical red lines) and UV (bars with horizontal blue lines) illumination towards (A) Rhodamine B and (B) Congo red.

Schematic 1. The electron transfer mechanism under visible light and the photocatalytic degradation of organic pollutants with the g-C_3N_4/CdS/RGO composite.

Table 1 The calculated reaction rate constants (min^{-1}) for P25, pure g-C_3N_4, g-C_3N_4/CdS, CdS/RGO, g-C_3N_4/RGO, and g-C_3N_4/CdS/RGO toward photodegradation of RhB and CR.

Table 2 Total organic carbon (TOC) analysis of dye solution, P25, pure g-C_3N_4, g-C_3N_4/CdS, CdS/RGO, g-C_3N_4/RGO, and g-C_3N_4/CdS/RGO after complete degradation under UV and VIS light irradiation ($\mu gC.L^{-1}$) toward photodegradation of RhB and CR. TOC for RhB and for CR dyes without photocatalysts, is provided for comparison.

Graphical abstract: Schematic of the electron transport from g-C_3N_4 to the CdS nanoparticles and RGO sheets during RhB photodegradation.

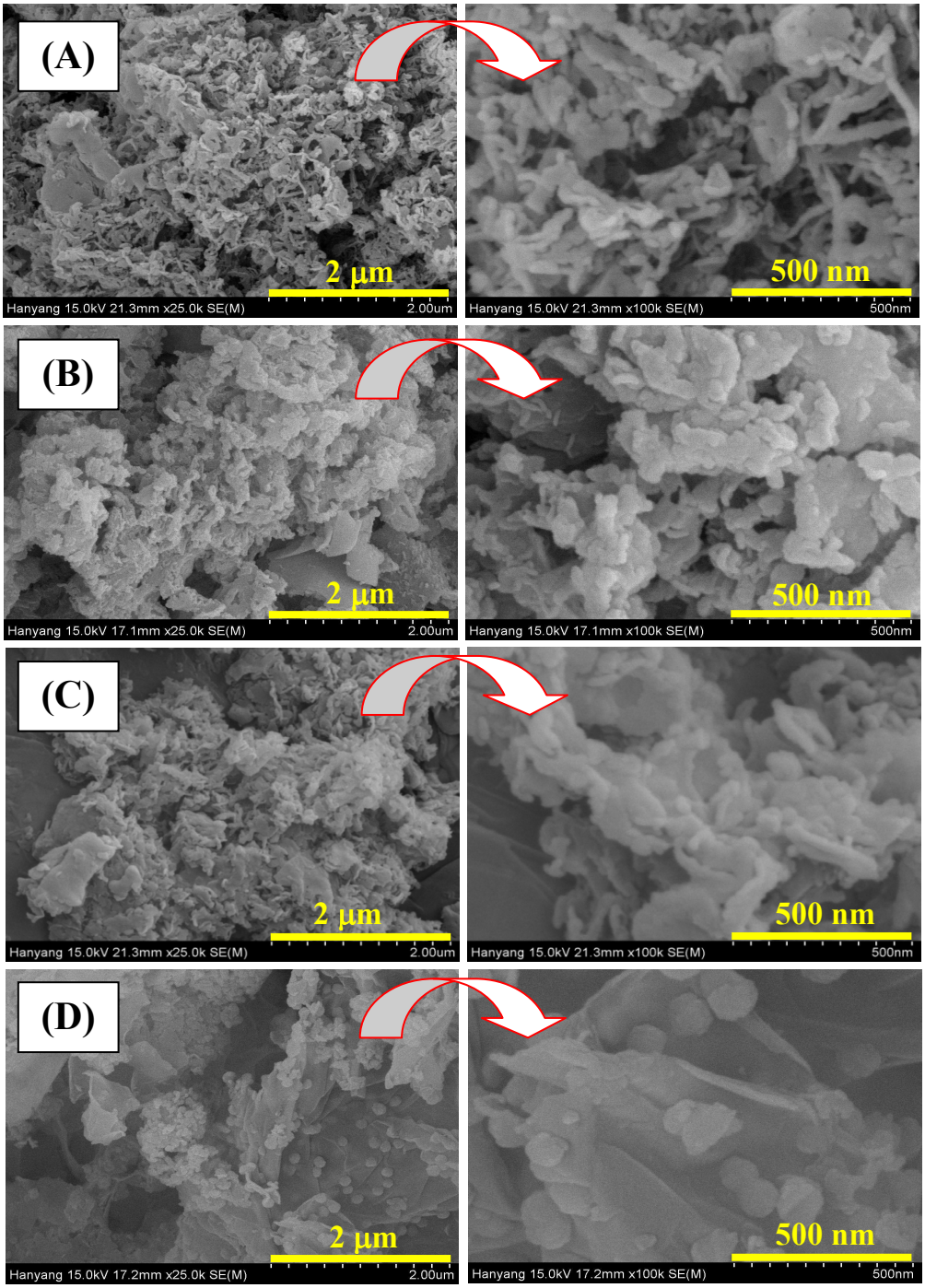

Figure 1

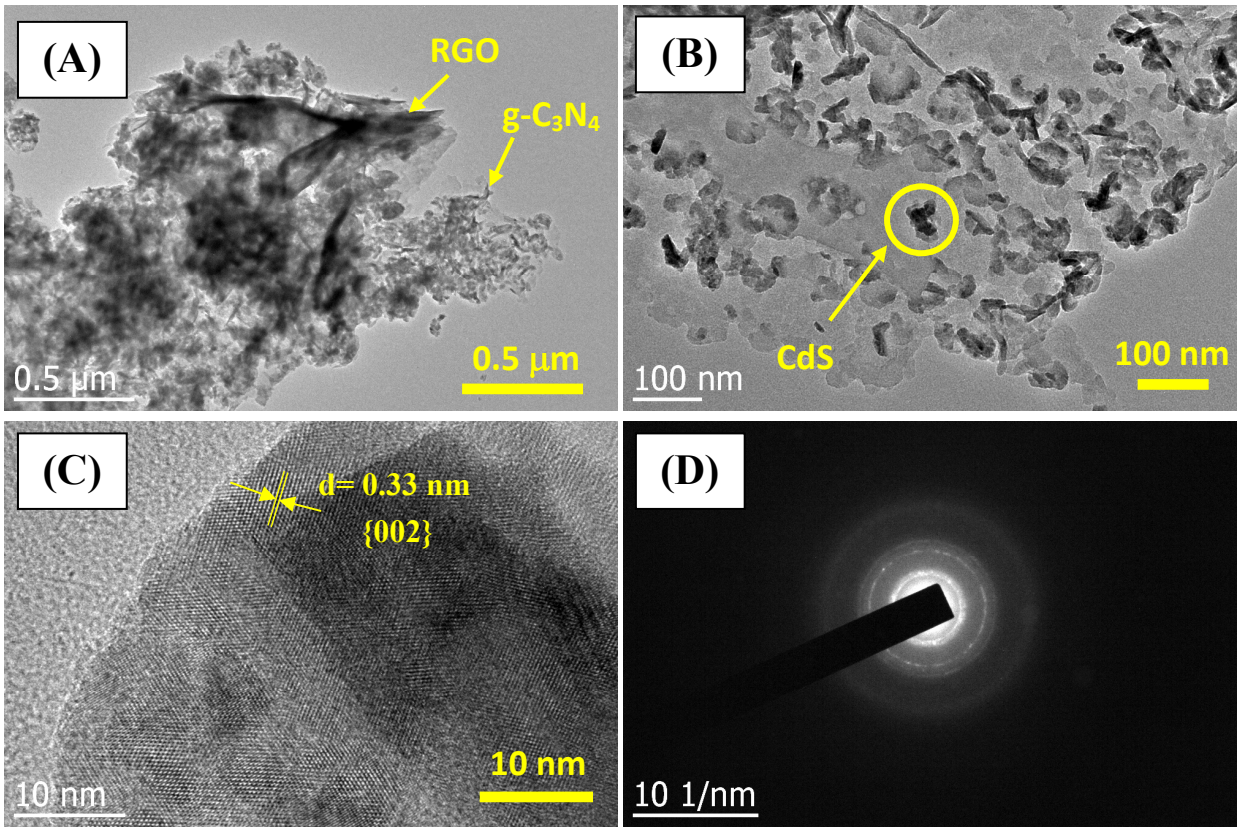

Figure 2

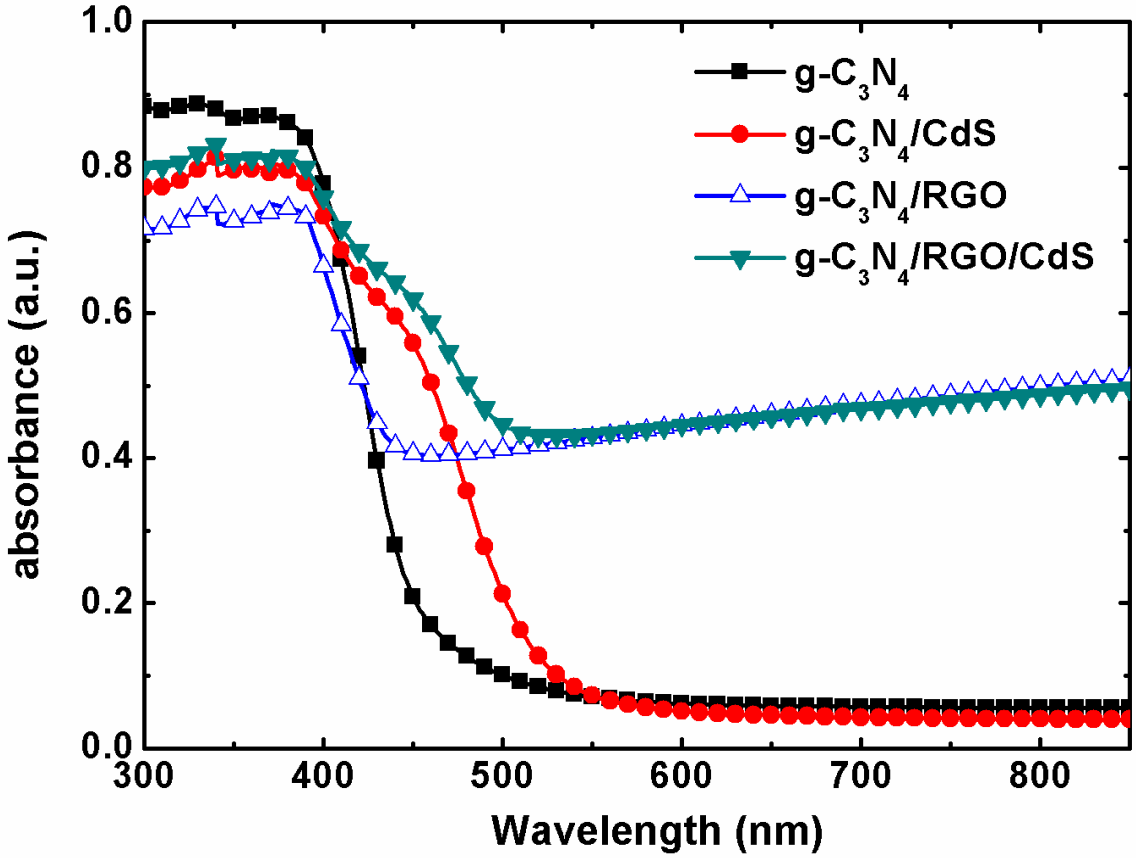

Figure 3

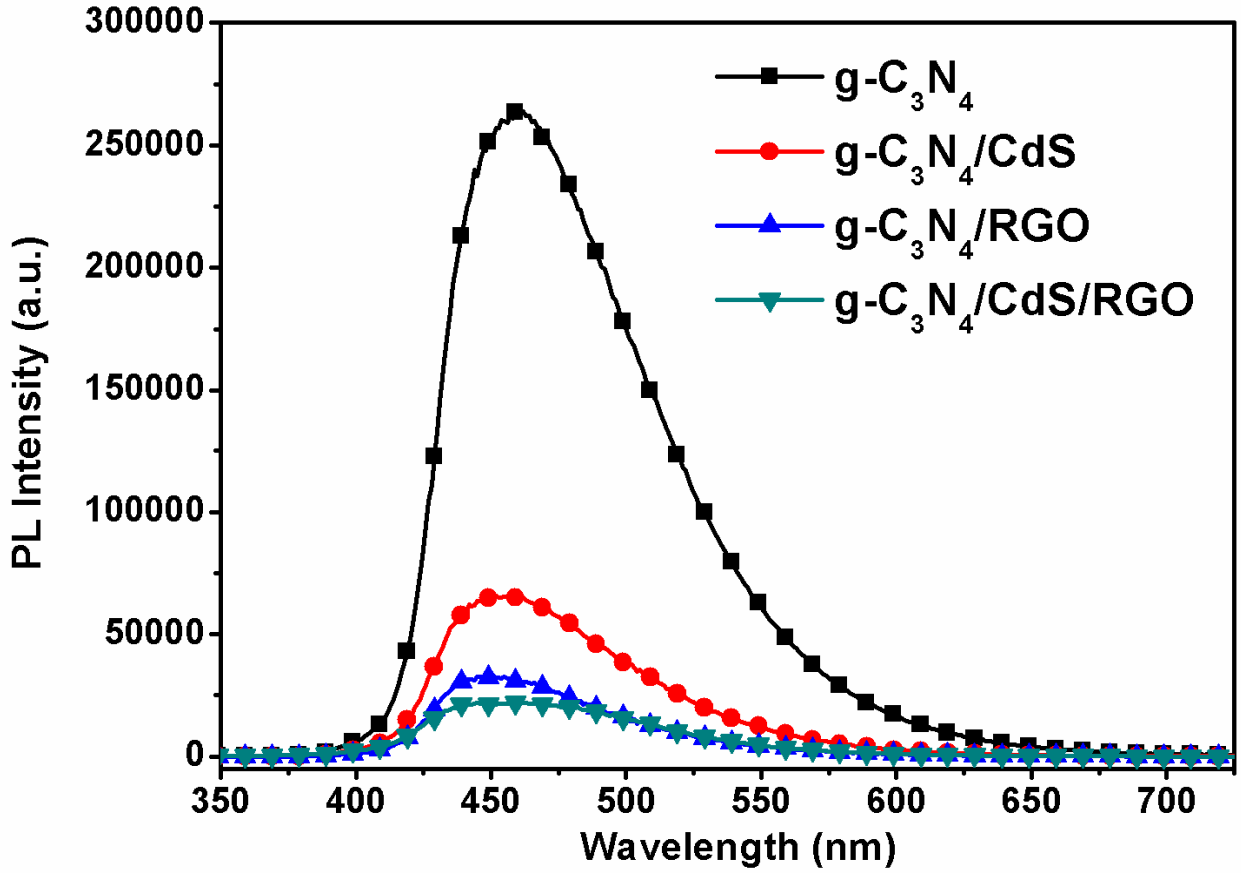

Figure 4

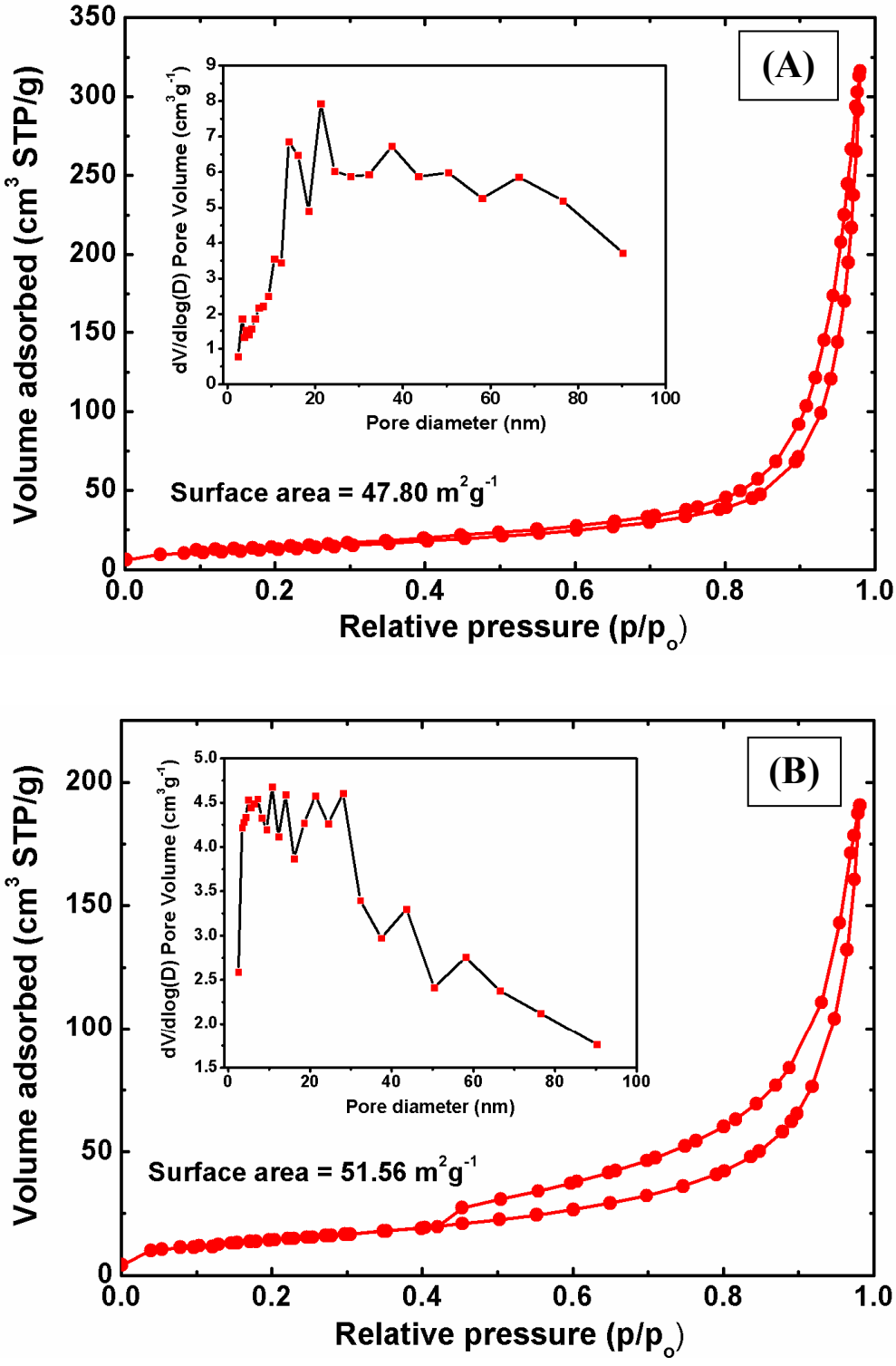

Figure 5(a and b)

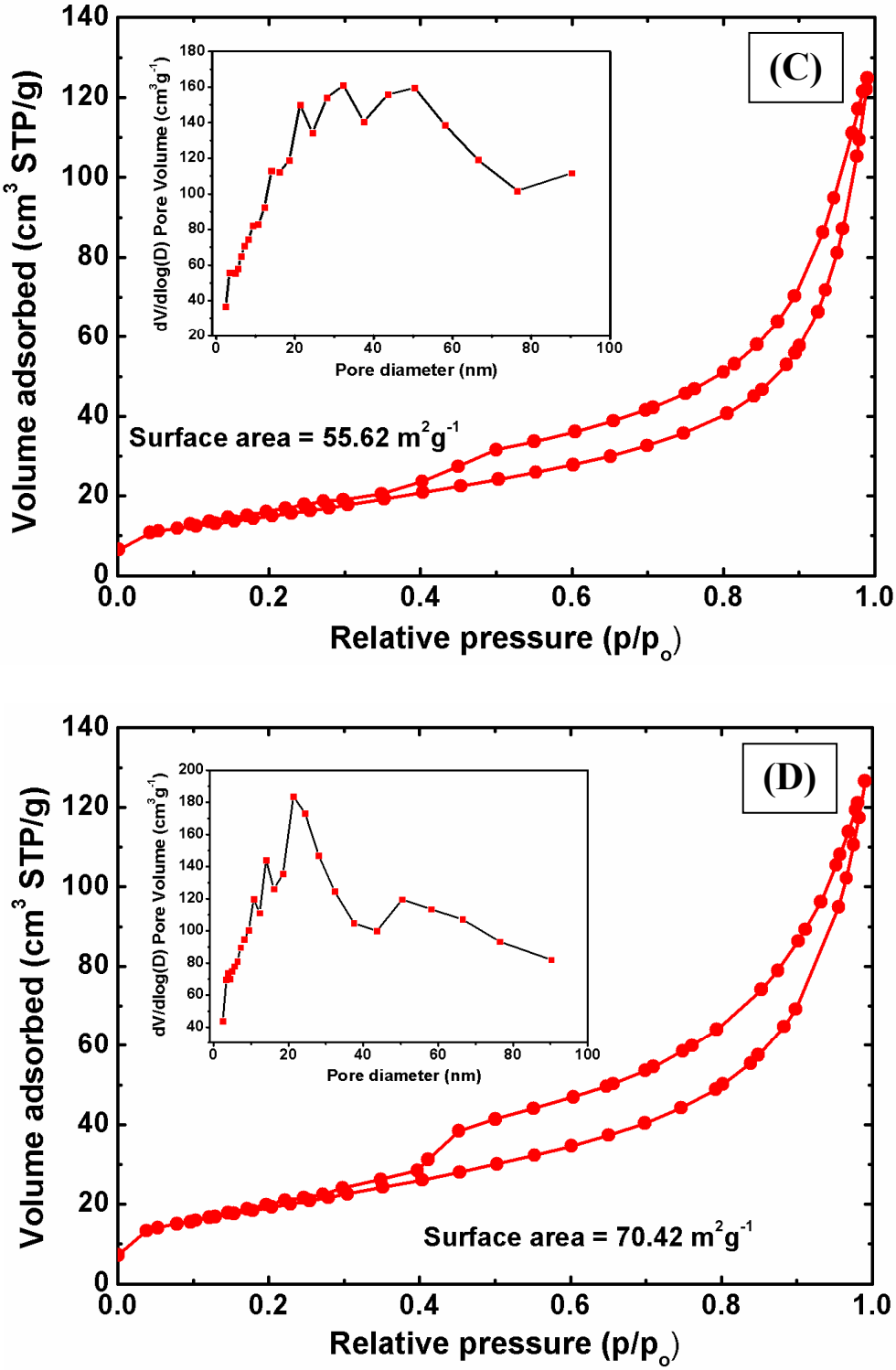

Figure 5(c and d)

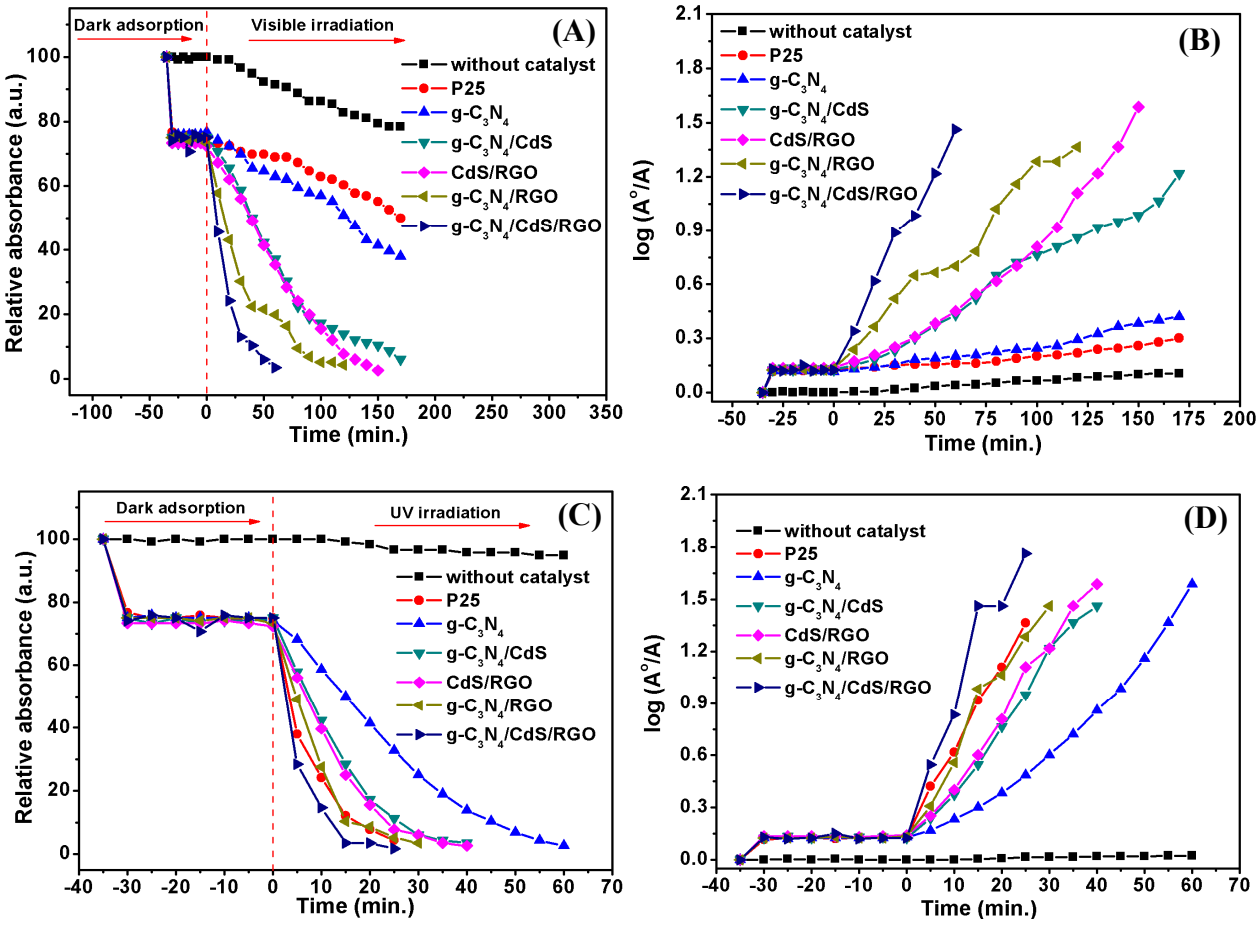

Figure 6(A to D)

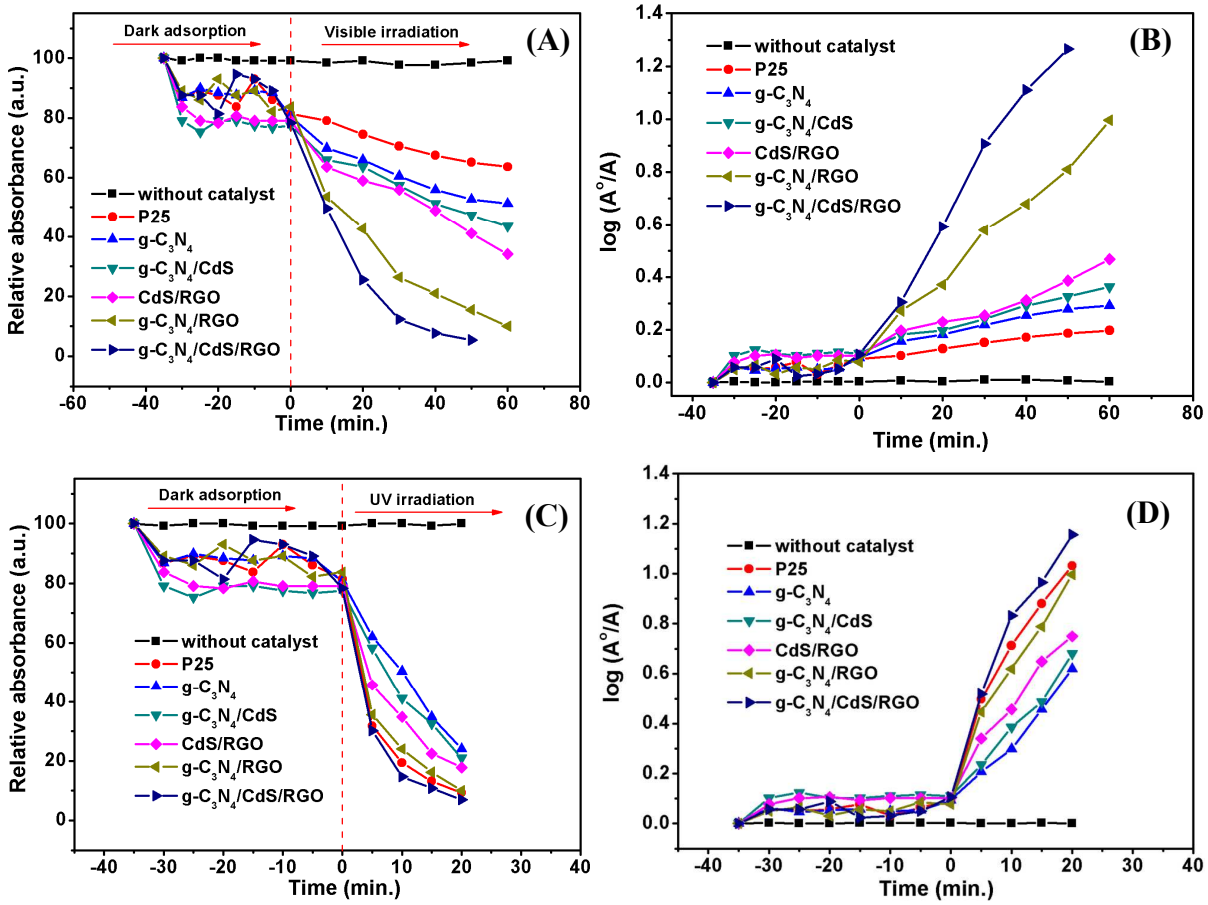

Figure 7(A to D)

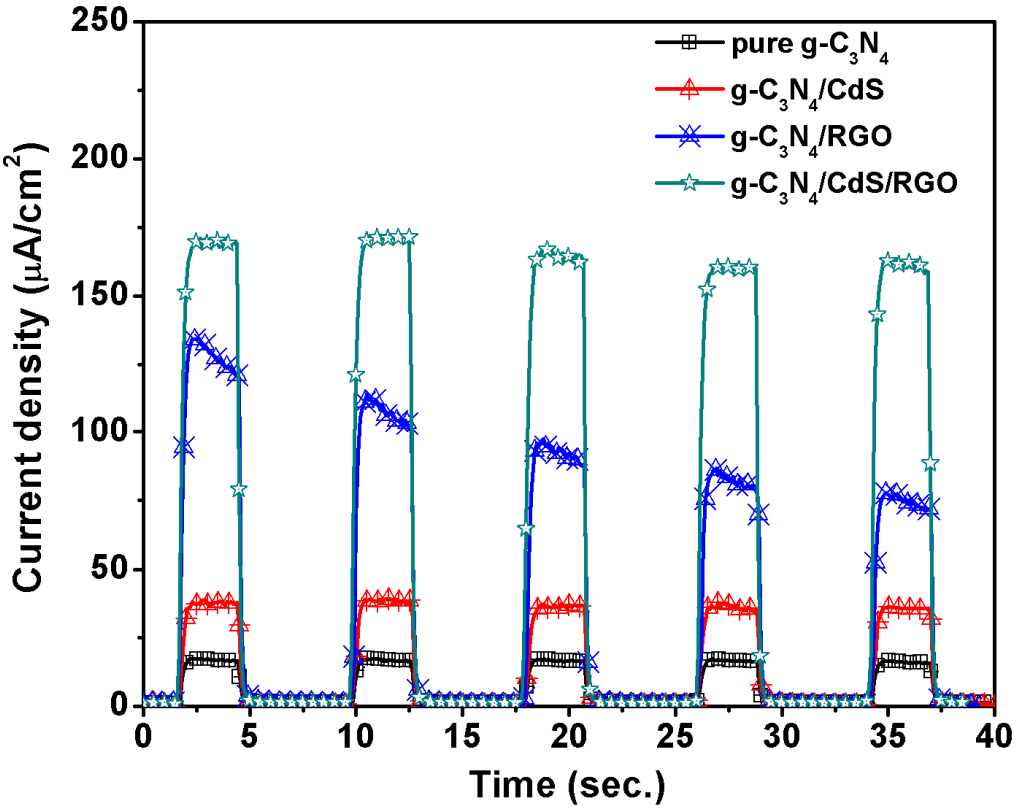

Figure 8

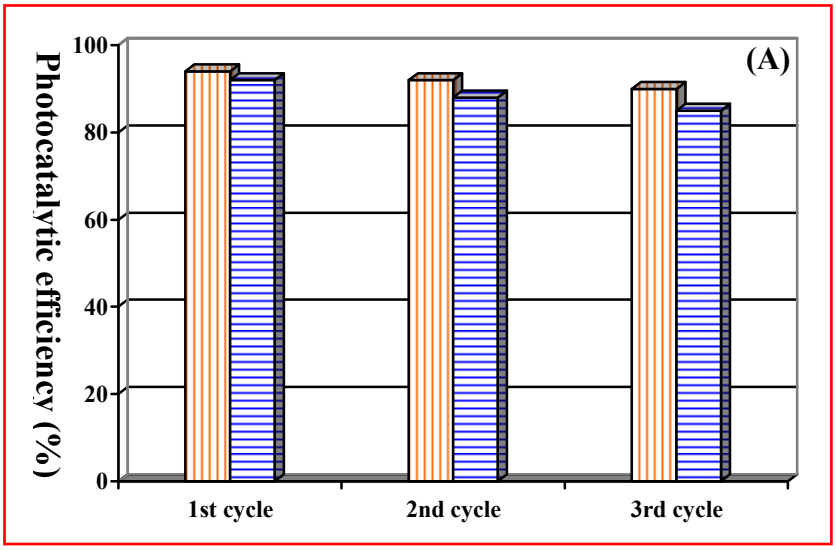

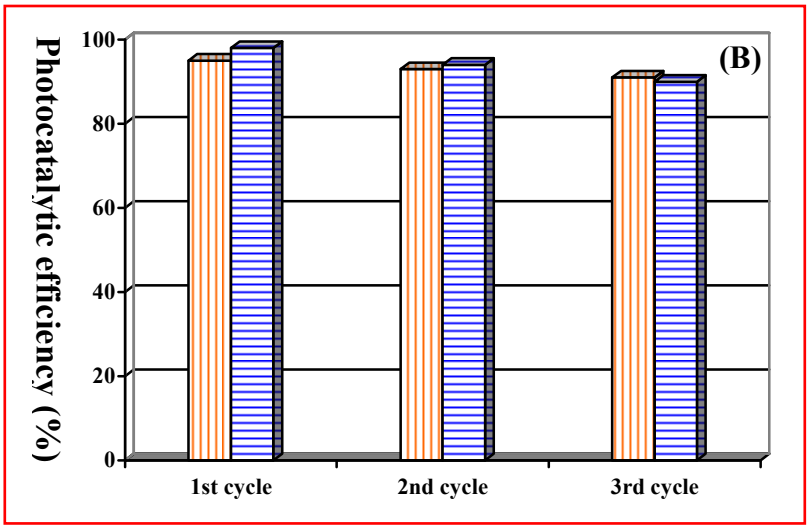

Figure 9 (A and B)

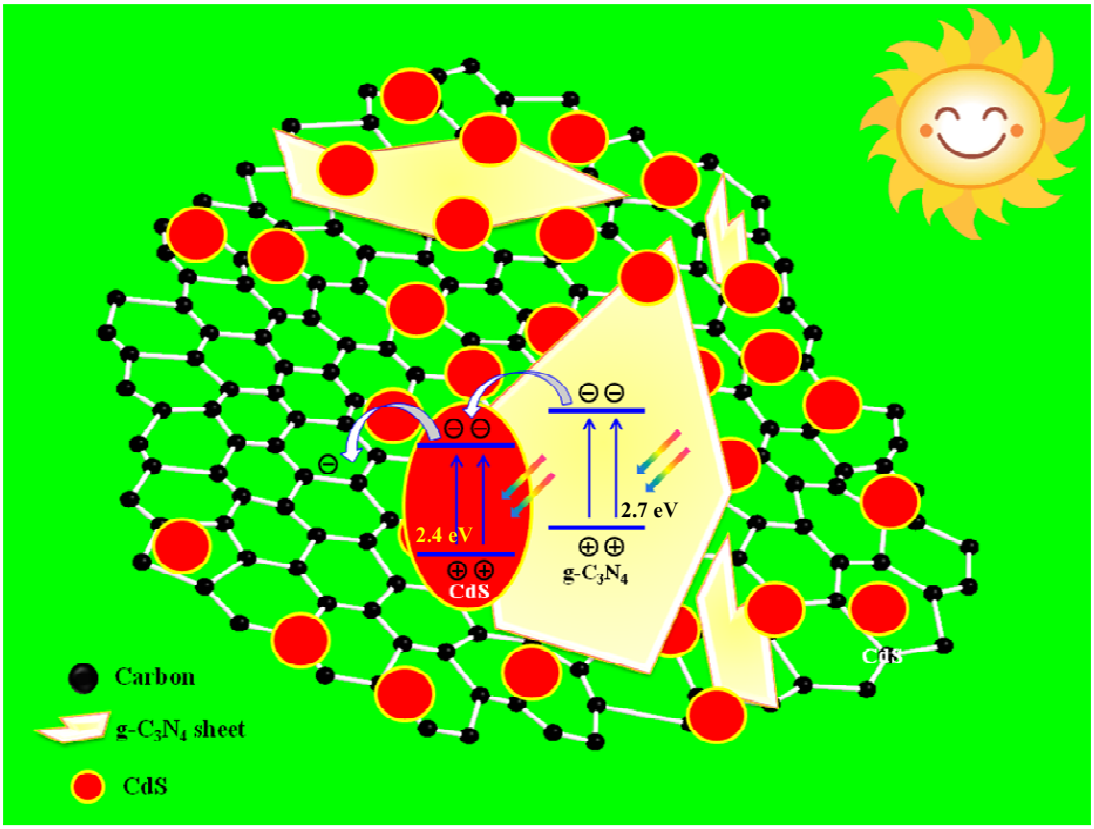

Schematic 1

Sample details	Kinetic rate constant (K x 10^{-3}) min^{-1} Rhodamine B		Kinetic rate constant (K x 10^{-3}) min^{-1} Congo Red	
	VIS	UV	VIS	UV
RhB	0.67	0.43	0.02	0.06
P25	0.96	48.98	1.91	45.33
g-C_3N_4	1.77	23.85	3.24	26.02
g-C_3N_4/CdS	6.43	36.09	4.06	28.78
RGO/CdS	9.31	38.55	5.56	32.04
g-C_3N_4/RGO	10.49	46.02	14.80	43.59
g-C_3N_4/CdS/RGO	21.92	66.12	24.37	50.90

Table 1

Sample details	TOC of Rhodamine B in μgCL^{-1}		TOC of Congo Red in μgCL^{-1}	
	VIS	UV	VIS	UV
Dye solution	22040	22040	25980	25980
P25	14317	1610	16248	1759
g-C_3N_4	11589	1936	14384	3971
g-C_3N_4/CdS	5794	1610	11942	3067
RGO/CdS	3612	1847	6482	2841
g-C_3N_4/RGO	1936	1737	2385	1951
g-C_3N_4/CdS/RGO	1685	1467	1821	1678

Table 2

Graphical abstract